Article

Dynamics of $K_2Ni_2(SO_4)_3$ governed by proximity to a 3D spin liquid model

Matías G. Gonzalez [1,2], Vincent Noculak[1,2], Aman Sharma [3], Virgile Favre[3], Jian-Rui Soh[3], Arnaud Magrez [4], Robert Bewley[5], Harald O. Jeschke [6,7], Johannes Reuther[1,2,7], Henrik M. Rønnow [3], Yasir Iqbal [7] & Ivica Živković [3]

Quantum spin liquids (QSLs) have become a key area of research in magnetism due to their remarkable properties, such as long-range entanglement, fractional excitations, and topologically protected phenomena. Recently, the search for QSLs has expanded into the three-dimensional world, despite the suppression of quantum fluctuations due to high dimensionality. A new candidate material, $K_2Ni_2(SO_4)_3$, belongs to the langbeinite family and consists of two interconnected trillium lattices. Although magnetically ordered, it exhibits a highly dynamical and correlated state. In this work, we combine inelastic neutron scattering measurements with density functional theory (DFT), pseudo-fermion functional renormalization group (PFFRG), and classical Monte Carlo (cMC) calculations to study the magnetic properties of $K_2Ni_2(SO_4)_3$, revealing a high level of agreement between experiment and theory. We further reveal the origin of the dynamical state in $K_2Ni_2(SO_4)_3$ to be centred around a magnetic network composed of tetrahedra on a trillium lattice.

QSLs are highly-entangled states of matter, in which no long-range magnetic order is observed, even in the absence of thermal fluctuations at zero temperature. Ever since P. W. Anderson's proposal of a resonating valence bond phase as the ground state for the triangular lattice Heisenberg antiferromagnet[1], QSLs have captured the attention of physicists across fields beyond quantum magnetism[2]. The reason lies in the wide range of exotic properties and phenomena that these intriguing states of matter display, ranging from fractionalization of spin excitations observed as an extended continuum in the excitation spectrum, to pinch-point singularities observed in the static spin-spin correlations and associated with U(1) QSLs or fracton phases[3–7].

The QSL behavior is driven by strong zero-point quantum fluctuations, which are enhanced in the presence of high magnetic frustration. This is realized either by competing isotropic interactions, as in

the Heisenberg model on the kagome lattice[8–10], or by anisotropic interactions, such as in the Kitaev model on the honeycomb lattice[11–13]. On the other hand, low dimensionality also amplifies quantum fluctuations, which are thus more noticeable in one- or two-dimensional systems. However, in recent years much attention has been put into three-dimensional (3D) models and compounds. Even though zero-point quantum fluctuations are greatly suppressed in 3D, highly frustrated systems like the network of corner-sharing tetrahedra realized by the pyrochlore lattice still provide a suitable environment for the existence of QSLs, both theoretically and experimentally[14–16]. Indeed, several compounds have been synthesized which realize pyrochlore, hyperkagome, or hyper-hyperkagome lattices and display QSL behavior in 3D[15,17,18]. Although often it is found that QSL candidate materials order at some finite-temperature T_N, their dynamic response is

[1]Helmholtz-Zentrum Berlin für Materialien und Energie, Hahn-Meitner-Platz 1, 14109 Berlin, Germany. [2]Dahlem Center for Complex Quantum Systems and Fachbereich Physik, Freie Universität Berlin, 14195 Berlin, Germany. [3]Laboratory for Quantum Magnetism, Institute of Physics, École Polytechnique Fédérale de Lausanne, CH-1015 Lausanne, Switzerland. [4]Crystal Growth Facility, École Polytechnique Fédérale de Lausanne, Lausanne, Switzerland. [5]ISIS Pulsed Neutron and Muon Source, STFC Rutherford Appleton Laboratory, Harwell Science and Innovation Campus, Didcot, Oxfordshire OX11 0QX, UK. [6]Research Institute for Interdisciplinary Science, Okayama University, Okayama 700-8530, Japan. [7]Department of Physics and Quantum Centre of Excellence for Diamond and Emergent Materials (QuCenDiEM), Indian Institute of Technology Madras, Chennai 600036, India. ✉e-mail: ivica.zivkovic@epfl.ch

strongly influenced by the proximity to a quantum critical point where the order completely disappears. The quantum critical regime, emanating from the quantum critical point, leaves its characteristic fingerprint in the dynamic response even at finite temperatures, as long as $T_N \ll |\theta_{CW}|$, where θ_{CW} is a Curie–Weiss temperature that defines the characteristic energy scale of the system. This allows testing theoretical predictions for QSLs in real materials, such as the existence of fractional excitations[19–21].

Recently, it has been shown that a new 3D magnetic network exhibits a highly dynamic ground state. $K_2Ni_2(SO_4)_3$, a member of the langbeinite family, develops spin correlations below 20 K between $S = 1$ moments, with a peculiar ordered state arising below ~1.1 K, freezing only around 1% of the available magnetic entropy and showing a tripling of the magnetic unit cell[22,23]. Furthermore, the application of $B = 4$ T magnetic field leads to a fully dynamical state down to the lowest temperatures. Another member of the langbeinite family, the $KSrFe_2(PO_4)_3$ compound with $S = 5/2$, was also claimed to exhibit spin-liquid behavior[24].

In this work, we combine both experimental and numerical methods to study the magnetic properties of $K_2Ni_2(SO_4)_3$ and its proximity to a spin-liquid model on a simpler lattice. We first perform density functional theory (DFT)-based energy mappings to obtain the Hamiltonian of the compound, taking into account its low-temperature structure. Using classical Monte Carlo (cMC) to study the magnetic ordering, we obtain the same tripling of the magnetic unit cell as observed experimentally. We then compare inelastic neutron scattering (INS) measurements with pseudo-fermion functional renormalization (PFFRG) calculations on the quantum $S = 1$ model, obtaining a good agreement. We finally trace the features observed in the spin structure factors to a nearby point in space which corresponds to a trillium lattice in which each triangle is turned into a tetrahedron. We analyze the spin-liquid properties of this tetra-trillium lattice and its surrounding areas in parameter space.

Results

Magnetic structure and Hamiltonian

The underlying magnetic network in these compounds comprises two interconnected trillium lattices, based on two symmetry-inequivalent magnetic sites, shown in Fig. 1a. Each trillium lattice with four sites per unit cell consists of a network of corner-sharing triangles where each site participates in three triangles (see Fig. 1b). For $K_2Ni_2(SO_4)_3$, our DFT-based energy mapping calculations reveal three dominant exchange interactions: J_3 and J_5 constituting nearest-neighbor couplings within each trillium lattice, and J_4 which couples the two trillium lattices (see the full list in Fig. 1a–c). In the limit $J_3, J_5 \to 0$, the network transforms into a bipartite lattice, supporting a semi-classical anti-ferromagnetic state. The limit $J_4 \to 0$ describes two independent trillium lattices, which have been theoretically investigated in detail[25,26] and shown to lead to a variant of the 120° order. Therefore, $K_2Ni_2(SO_4)_3$, with its magnetically highly correlated and dynamical state, represents a surprising revelation that indicates the proximity to an island of liquidity that has escaped the attention of the scientific community so far.

While previous coupling values were reported for the room-temperature structure[22], here we propose a new set of parameters calculated by DFT energy mapping based on a refined crystal structure at $T = 100$ K (see Supplementary Notes 1 and 2). The new values of exchange interactions (listed in Fig. 1a) are moderately renormalized compared to the room-temperature structure values but show the same hierarchy of interactions $J_4 > J_5 > J_3 > J_1 > |J_2|$, where J_2 is the only ferromagnetic coupling. Specifically, room-temperature couplings relative to the dominant $J_4 = 5.545$ K are $J_1 = 0.079J_4$, $J_2 = -0.030J_4, J_3 = 0.203J_4, J_5 = 0.472J_4$, and for the $T = 100$ K structure they become $J_1 = 0.066J_4, J_2 = -0.026J_4, J_3 = 0.144J_4, J_5 = 0.479J_4$. The most significant difference occurs for J_3, which changes by ~30%. Even though $K_2Ni_2(SO_4)_3$ orders at about 1.1 K, the state seems to remain predominantly dynamic, with the persistence of the diffuse scattering
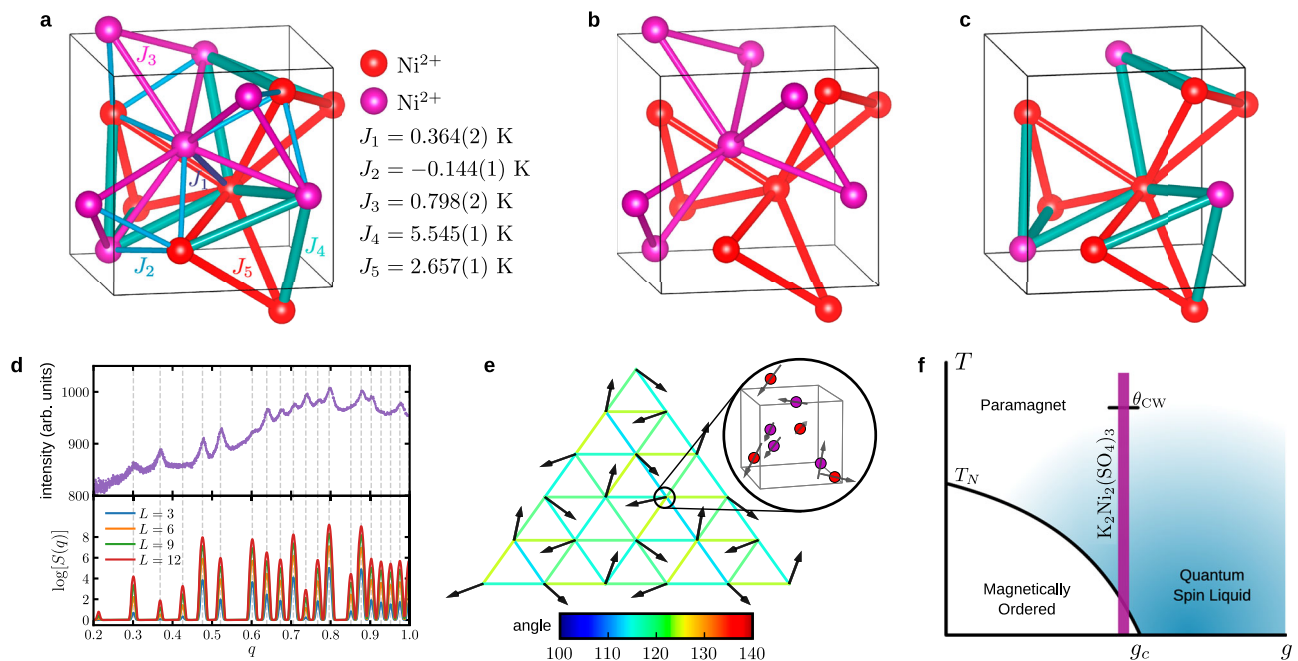

Fig. 1 | Crystal and magnetic structure of $K_2Ni_2(SO_4)_3$. a Two trillium lattices of Ni^{2+} ions in $K_2Ni_2(SO_4)_3$ with the five nearest-neighbor couplings calculated by DFT energy mapping. **b** J_3 and J_5 form two independent trillium lattices. **c** J_4 couples each ion from one trillium lattice to the nearest triangle of the second trillium lattice. For $J_4 = J_5$, magnetic ions form a network of corner-shared tetrahedra based on a trillium lattice, a tetra-trillium lattice. **d** Spin structure factor $S(q)$ as a function of $q = |\mathbf{q}|$. Comparison between cMC calculations at $T = 0$ for the DFT model (bottom) and

diffraction data at 100 mK taken from ref. 22 (top). A small Gaussian broadening is used for the cMC results. **e** The spin structure corresponding to the tripled magnetic unit cell determined by cMC is shown in a cut along the (111) plane for an $L = 6$ system. Black arrows represent the direction of the sum of moments within a single unit cell. The bond color indicates the angle between the unit cell moments. **f** Schematic of the proximity of the $K_2Ni_2(SO_4)_3$ Hamiltonian to a spin-liquid region and its effect at finite temperatures, where g is a function of the couplings J_i.
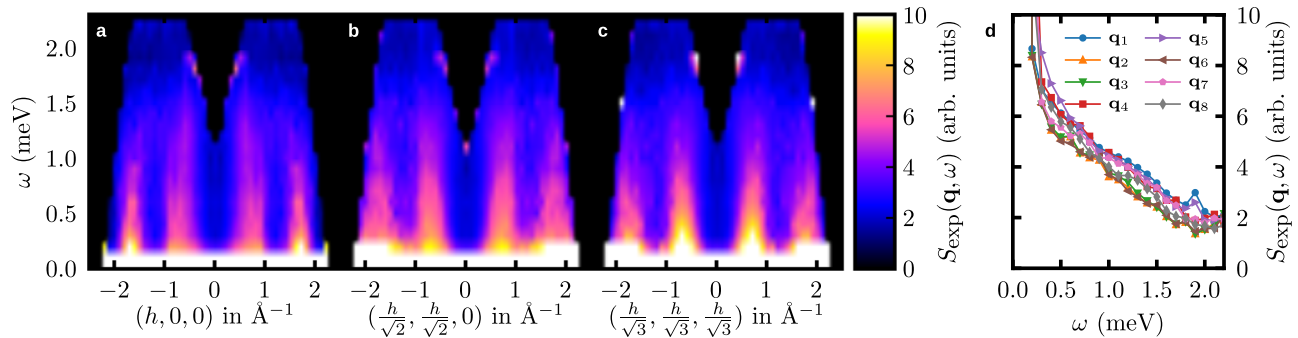
Fig. 2 | Time-of-flight neutron scattering on single crystals of $K_2Ni_2(SO_4)_3$. Energy ω versus wave vector **q** for **a** **q** = (100), **b** **q** = (110) and **c** **q** = (111) directions. **d** Energy dependence of the dynamical structure factor $S_{exp}(\mathbf{q},\omega)$ obtained at several **q**-points (for which streaks of intensity are observed), revealing a monotonous decrease of intensity towards the high-energy background. **q**-points are: $\mathbf{q}_1$ = (0.50, 0.50, 0.00), $\mathbf{q}_2$ = (0.00, 1.70, 0.00), $\mathbf{q}_3$ = (0.65, 0.00, 0.00), $\mathbf{q}_4$=(1.20,1.35,0.00),$\mathbf{q}_5$=(0.50,0.50,0.50),$\mathbf{q}_6$=(1.70,0.00,0.00),$\mathbf{q}_7$=(0.00,1.65,1.65),$\mathbf{q}_8$ = (1.05, 1.40, 1.40).

and absence of magnon branches[22,23]. This makes it impossible to use the more standard approach for determining the exchange interactions, which relies on comparing the magnon dispersion with spin-wave theory (SWT). Furthermore, the magnetic unit cell consists of 216 spins, which represents a significant challenge for SWT. Alternatively, one could perform the comparison in the magnetic field-polarized state, where the magnetic order is trivial for SWT. However, the required polarizing magnetic field for $K_2Ni_2(SO_4)_3$ can be estimated to reach 25–30 T, and is therefore out of the reach of the current state-of-the-art facilities for INS measurements.

Even though the different sets of exchange parameters J_1-J_5 proposed for $K_2Ni_2(SO_4)_3$ are not very different, the magnetic order does change depending on the choice. To evaluate this, we perform cMC calculations on periodic systems consisting of L^3 unit cells, where L is the linear size of the system. Because this method is best suited to detect classical magnetic orders in the absence of quantum fluctuations, it allows us to validate/invalidate the different Hamiltonians by comparing them to neutron scattering measurements below the critical temperature.

All our classical calculations indicate a transition to a magnetically ordered phase at finite temperatures. However, the lowest ground-state energy is only reached for $L = 3n$ lattices (with critical temperature $T_c^{cMC}/J_4 = 0.048(2)$), while all other sizes ($L \neq 3n$) give higher energies at $T = 0$, implying that the magnetic order is frustrated by periodic boundary conditions. The magnetic orders obtained for $L = 12, 9, 6$, and 3 are all identical, indicating a tripling of the magnetic unit cell and a perfect agreement with the Bragg points observed experimentally (Fig. 1d). Interestingly, if the DFT Hamiltonian corresponding to the room-temperature structure is used[22], the $L = 4n$ magnetic order has the lowest energy (only 0.09% below $L = 3n$), indicating a very sensitive landscape of complex magnetic configurations. Another recently suggested set of values with $J_3 = 0$[23] leads to a quintupling of the magnetic unit cell, exhibiting the lowest ground-state energies for $L = 5n$ lattices. These calculations evidence not only that it is not trivial to capture the experimentally observed Bragg structure[22], but also give a certain level of confidence for the set of exchange interactions determined here based on the structure at 100 K.

The cMC magnetic structure for $L = 3n$, shown in Fig. 1e, comprises propagation vectors q_1 = (1/3, 0, 0), q_2 = (1/3, 1/3, 0) and q_3 = (1/3, 1/3, 1/3). The resulting pattern is devoid of any particular spin textures like skyrmions and merons. In Fig. 1e, we show a view along the (111) plane for a $L = 6$ system, where black arrows on each node represent the direction of the net magnetic moment within each unit cell. The angles between neighboring

cells are found to be close to 120°. We do not expect a significant change in the calculated structure if the exchange parameters are slightly modified, as long as the tripling of the unit cell is preserved.

We should point out that the agreement between cMC and the weak magnetic Bragg scattering serves only to narrow down the appropriate set of Js. The ordered state in $K_2Ni_2(SO_4)_3$ remains highly dynamic down to the lowest temperatures[22,23] and exactly how the weak static component emerges from a highly dynamic background remains to be investigated in future studies. A similarly strong dynamic ground state, with faint features of spin-glass order, has been observed in $Tb_2Hf_2O_7$[27], with spin-liquid-like dynamics observed down to the lowest temperatures. In the rest of this work, we focus on temperatures above the ordering ($T = 2$ K) but significantly below the characteristic energy of the system (θ_{CW} = -18 K). In this case, the dynamic features above the ordering trace their origin to a region proximate in parameter space that exhibits purely spin-liquid characteristics and shows no magnetic order down to $T = 0$, as illustrated in Fig. 1f. Although the dynamics observed below the ordering temperature in $K_2Ni_2(SO_4)_3$ could potentially be also dominated by the spin-liquid-like features, as found for $Tb_2Hf_2O_7$, it is also important to realize that entering the ordered state can significantly redistribute the scattering spectral weight, and often completely remove the spin-liquid features.

Dynamic and static spin structure factors

To characterize the dynamical features in $K_2Ni_2(SO_4)_3$, we have conducted INS experiments in three different directions within the (HLL) scattering plane. In Fig. 2, we present experimental results for the dynamical structure factor $S_{exp}(\mathbf{q}, \omega)$ with the incident energy $E_i = 2.8$ meV obtained at 2 K, significantly above the appearance of order to avoid possible quasi-elastic scattering but well within the dynamical state. Energy-momentum plots along three principal directions show vertical streaks of intensity, four in each panel, indicating a non-dispersive type of excitations. The streaks are centered ~0.75 and 1.8 inverse units, and are very broad, excluding the possibility of a quasi-elastic scattering from ordering that would appear in a much denser grid at multiples of 1/3 of the unit cell[22,23]. The streaks are present both below and above the ordering, and their intensity fades very slowly towards high temperatures[23]. The upper energy bound of excitations is found to be ~2 meV, in agreement with the onset of correlations in specific heat below 20 K[22]. The energy dependence of the intensity of the scattering signal for various **q**-points found in the middle of broad peaks is featureless, with an approximately linear decreasing dependency on the energy (see Fig. 2d). Such **q**- and ω-dependence of the scattering intensity $S(\mathbf{q}, \omega)$ allows us to estimate the equal-time
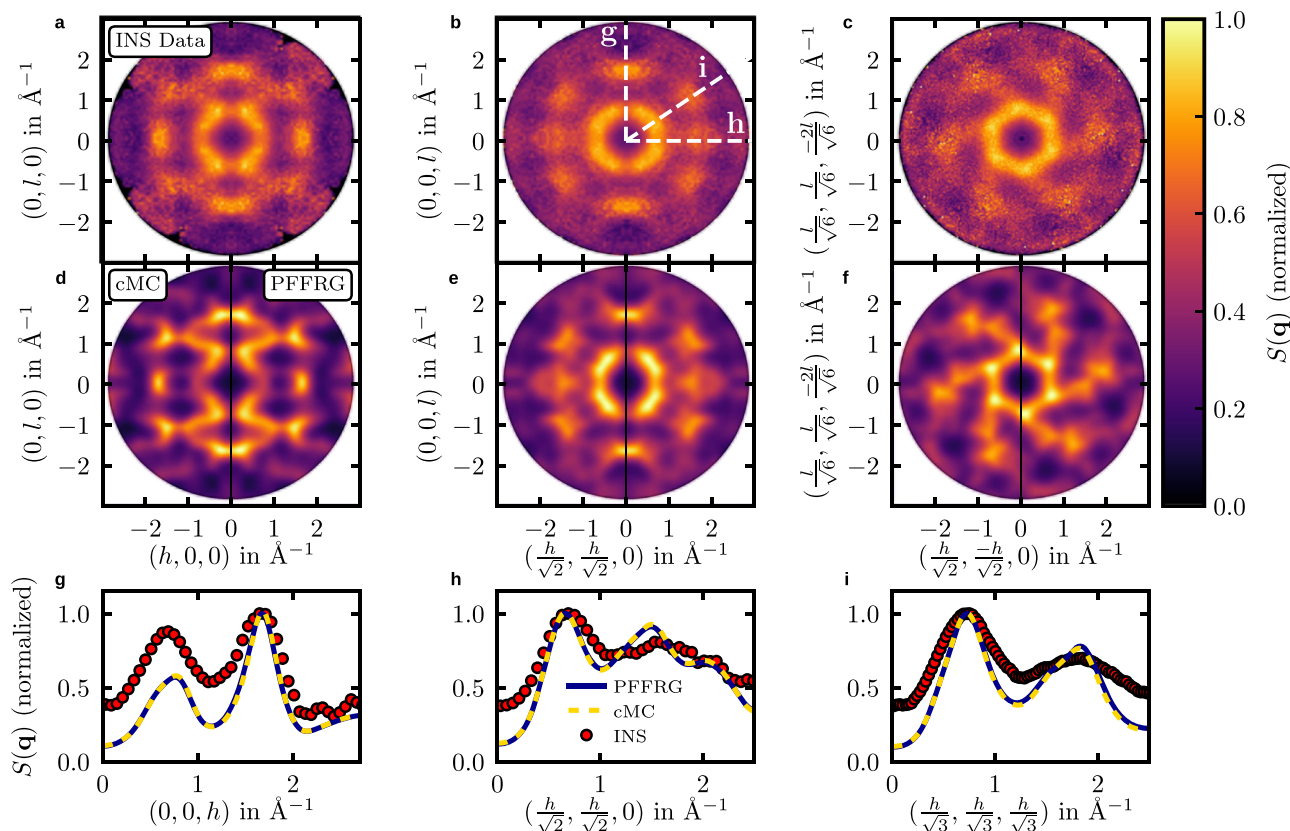
Fig. 3 | Comparison of experimental and theoretical spin structure factors. Spin structure factor $S(\mathbf{q})$ along different planes in reciprocal space (normalized by its maximum value within the plane, unless specified otherwise). **a–c** experimental data obtained by INS with the incident energy $E_i = 5.0$ meV, integrated in the range from 0.5 meV to 1.0 meV. In this case, the data is normalized by an arbitrary value of 11. **d–f** cMC calculations at $T = 0.35 J_4$ (left half) and PFFRG calculations for $\Lambda = 0.58 J_4$ (right half), using the form factor of Ni^{2+} ions. **g–i** line cuts along three principal directions indicated by white dashed lines in **b**.

magnetic structure factor

$$S_{\exp}(\mathbf{q}) \sim \int_{\omega_1}^{\omega_2} S_{\exp}(\mathbf{q}, \omega) \, d\omega \qquad (1)$$

which can then be directly compared with theoretical predictions based on a given spin Hamiltonian. We note that a comparison on the level of $S(\mathbf{q}, \omega)$ would be far from trivial, even within the ordered state due to multiple ordering vectors and 216 spins per magnetic unit cell. Additionally, SWT is by construction applicable for small deviations from a classical order; and in the case of $K_2Ni_2(SO_4)_3$, the deviations from the classical order cannot be taken as small perturbations, rendering it practically outside of the scope of a reliable application of a SWT. Finally, the ordered state of $K_2Ni_2(SO_4)_3$ proves to be rather peculiar, marked by only 1% of entropy release and weak magnetic Bragg scattering[22]. Other characteristic features of classical order, like oscillations in μSR and magnon dispersions, are completely absent[22,23].

In Fig. 3a–c, we show the spin structure factor $S_{\exp}(\mathbf{q})$ along three different planes in reciprocal space, obtained by integrating the intensity in the energy range from $\omega_1 \sim E_{\min} = 0.5$ meV to $\omega_2 \sim E_{\max} = 1$ meV. The extent of the incoherent scattering gives the lower limit, while the upper limit is found as an optimal value to maximize the signal-to-noise ratio. The patterns depicted carry fingerprints from the underlying magnetic lattice composed of two interconnected trillium lattices, with a hexagonal galaxy-like motif reflecting the chirality of the crystal structure (see Fig. 3c), arising from the non-centrosymmetric space group.

To reproduce these experimental patterns, we performed calculations using both quantum and classical approaches. In the quantum limit, we use PFFRG, which has been shown to produce accurate results

in highly frustrated systems[28–32]. Within PFFRG, the renormalization-group flow is controlled by the cutoff frequency Λ, which is lowered from the interactions-free limit $\Lambda = \infty$ where the solution is known (see Supplementary Note 4). In this case, the flow breaks at $\Lambda = 0.582 J_4$, indicating the presence of a magnetically ordered ground state. As is standard for the PFFRG calculations, the static spin correlations are measured slightly above the flow breakdown and, even though calculations are carried out at $T = 0$, the finite value of the renormalization-group parameter Λ produces an effect similar to finite temperature[33]. In an attempt to also simulate the experimental data using cMC, we perform calculations above the finite-temperature phase transition. We find an excellent agreement with the PFFRG calculations for a large range of temperatures and, particularly for $T = 0.35 J_4$, we find the best quantitative agreement (see Fig. 3d–f). This quantum-to-classical correspondence at the level of static correlators has been previously reported in several frustrated 2D and 3D spin-1/2 Heisenberg models at finite temperatures[34–36], some of which host a QSL ground state. However, it is important to note that this correspondence does not hold for the full dynamical spectrum of the models, which are different in quantum and classical systems. Very recently, it has been shown through perturbation theory that the quantum-to-classical correspondence breaks at fourth order in J/T, even though partial diagrammatic cancellations lead to good accuracy even at low temperatures[37].

A more detailed comparison is obtained along the line cuts shown in Fig. 3g–i. As is evident from all three plots, there is very little difference between cMC and PFFRG results, upholding the quantum-to-classical correspondence. On the other hand, the agreement with the experiments is excellent in terms of the determination of peaks in the spin structure factor, which gives rise to pattern matching in the color
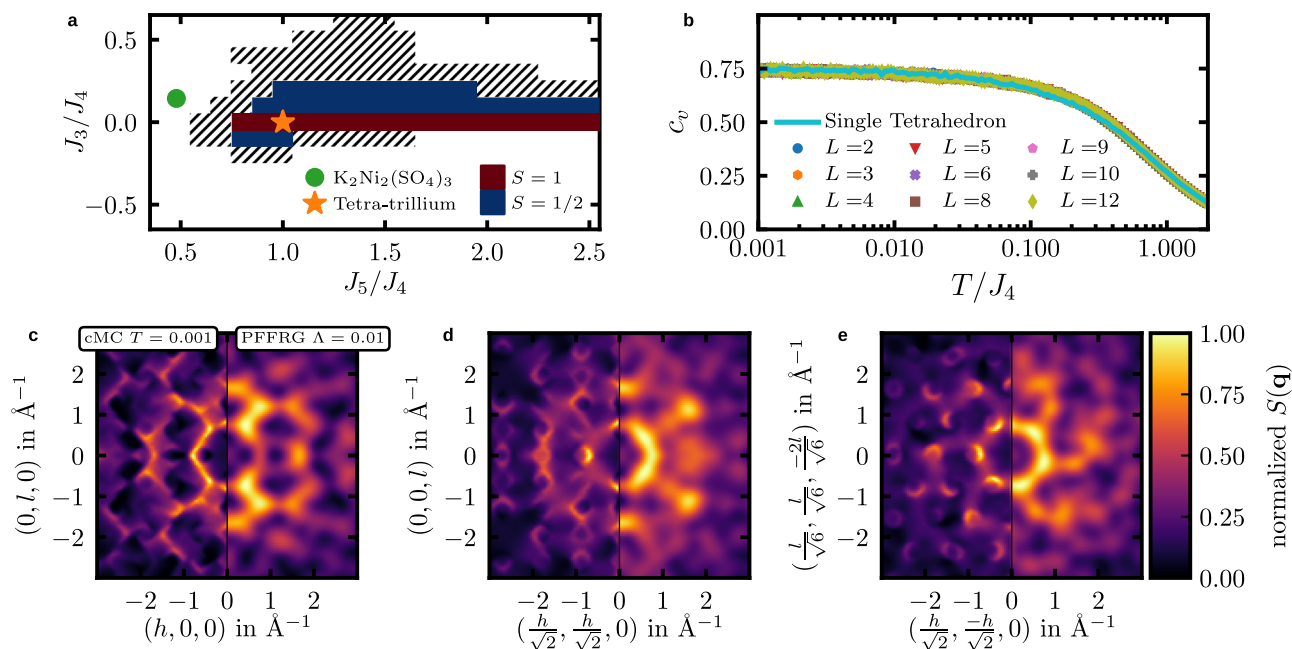
Fig. 4 | The island of liquidity around the tetra-trillium lattice. a PFFRG correlated paramagnetic region, indicating no long-range order at $T = 0$, for $S = 1/2$ (red +blue) and $S = 1$ (red). The dashed part indicates the region where the existence of a flow breakdown is hard to determine for the $S = 1/2$ model. The green circle and orange star indicate the DFT model for $K_2Ni_2(SO_4)_3$ and the tetra-trillium lattice plots. limit, respectively. **b** cMC calculations for the tetra-trillium lattice limit show no finite-size effects in the specific heat. Data for a single tetrahedron is also shown in a light-blue line. **c–e** Spin structure factor $S(\mathbf{q})$ using cMC and PFFRG calculations for the tetra-trillium lattice on different planes at $T = 0.001 J_4$ and $\Lambda = 0.01 J_4$, respectively.

Deviations can be seen in terms of the predicted ratio of intensities of two principal peaks along [100] and [111], the width of peaks, as well as a qualitative difference at large q along [110]. At least partially, these deviations could be explained by the limitations of the finite energy range integration used in Eq. (1). A more thorough comparison would require a full theoretical description of $S(\mathbf{q}, \omega)$. However, given the highly frustrated 3D network, the large unit cell, and the spin value $S = 1$, these calculations are beyond the reach of current theoretical methods. Despite this, we have shown that our theoretical description of $K_2Ni_2(SO_4)_3$ captures all the main aspects of its magnetism, covering both static and dynamic elements. That is to say, the DFT Hamiltonian we derived solely from the atomic positions enables us to reproduce the experimental Bragg structure and the magnetic unit cell below the phase transition (Fig. 1d) as well as the spin structure factor obtained by INS measurements above the ordering (Fig. 3a–c).

Proximity to a spin liquid

Due to the complexity of the underlying 3D magnetic network, with the classical limits for $J_3, J_5 \rightarrow 0$ and $J_4 \rightarrow 0$, it is far from evident why it is so geometrically frustrated in the case of $K_2Ni_2(SO_4)_3$. Simpler networks with similar classically ordered ground states, like the square or triangular lattices, are very susceptible to the introduction of additional frustrating couplings which eventually drive them to spin-liquid states ($J_2/J_1 \sim 0.5$ and $J_2/J_1 \sim 0.06$ for the square[38–43] and triangular lattice[44–49], respectively, even though other non-magnetic states have been proposed for the square case[50]). In the context of a large variety of different compounds with the same structure, belonging to the langbeinite family, it represents an important task to pinpoint the source of the observed frustration. To this end, we have studied a wider range of the J_3-J_4-J_5 parameter phase space with both PFFRG and cMC calculations. It turns out that the set of exchange parameters characterizing $K_2Ni_2(SO_4)_3$ lies very close to a so-far unexplored region where long-range magnetic order appears to be completely absent, centered around a particular point defined by $J_3 = 0, J_4 = J_5$. In this limit, the lattice is composed of corner-sharing tetrahedra with every ion

from one trillium lattice connected to the sites of the nearest equilateral triangle from the second trillium lattice (Fig. 1b), and therefore we call it a tetra-trillium lattice. In this lattice, half of all spins (i.e., those from one trillium lattice) are shared by three tetrahedra, while the remaining half (from the other trillium lattice) belongs to only one tetrahedron. Calculations performed in this limit do not show any signs of magnetic ordering in both classical $S \rightarrow \infty$ (down to $T = 0.001 J_4$) and extreme quantum $S = 1/2$, 1 limits (down to $\Lambda = 0.01 J_4$) (see Supplementary Note 4), providing indications of spin-liquid behavior in both the classical and quantum limits.

The extent of the island of liquidity around the tetra-trillium lattice (indicated by the orange star in Fig. 4a), however, depends strongly on the spin value considered. For $S = 1$, PFFRG indicates a very narrow range around $J_3 = 0$, with an extended set of values along the J_5/J_4 axis exhibiting a dynamical ground state, ranging from -0.8 up to -3.5. On the other hand, the $S = 1/2$ case exhibits the absence of magnetic order for $J_3 \neq 0$ for certain values of J_5/J_4 and extends up to larger J_5/J_4 below the pure trillium lattice limit $J_3 = J_4 = 0$. The wider area indicated by the line pattern in Fig. 4a indicates a region where it is numerically hard to determine the existence of a breakdown in the Λ-flow for the $S = 1/2$ case. Even beyond this region, the flow breakdowns are quite subtle, indicating weakly ordered phases. The set of parameters calculated with DFT for $K_2Ni_2(SO_4)_3$, indicated by a green circle in Fig. 4a, lies close to these putative spin-liquid regions. This becomes evident when the PFFRG spin structure factors from Fig. 3 are compared to the results obtained in the tetra-trillium lattice limit (at $\Lambda = 0.01 J_4$) shown in Fig. 4c–e, as many of the features can be put in correspondence. Generally, the peaks become more smeared in the tetra-trillium limit, but there is no indication of a strong difference between the two phases. This provides evidence that the properties of $K_2Ni_2(SO_4)_3$ are governed by its proximity to the QSL phase in the tetra-trillium lattice[19,20].

In analogy to quantum spin ice, where a QSL arises out of a classical spin liquid (CSL) when adding quantum fluctuations, we address here the question of whether the classical tetra-trillium lattice also

hosts a CSL which can potentially turn into a QSL when adding quantum fluctuations. The first indication is that cMC calculations show no ordering tendencies down to the lowest temperatures. However, a more conclusive proof of the CSL ground state in the classical limit can be constructed as follows. First, the Hamiltonian can be written as a disjoint sum of squared total spin in each tetrahedron (just as for the pyrochlore lattice). With this re-writing, the classical ground-state energy can be found exactly, given that a solution with zero net magnetic moment in each tetrahedron exists. This solution cannot exist for $J_5/J_4 < 1/3$, providing a theoretical limit (which we confirmed with cMC calculations). Second, for the tetra-trillium lattice, we confirmed that a collinear solution exists (which is also a solution of the Ising model) and clusters of 18 spins can be systematically found and flipped while conserving the property of vanishing total spin in each tetrahedron (see Supplementary Note 6). This allows the system to move through an extensive ground-state manifold and confirms the liquidity of this phase. Compared to the pyrochlore lattice, more spins are needed to construct a minimal flippable cluster because of the ramifications that occur at sites shared by three tetrahedra in the tetra-trillium lattice. When adding other couplings such as J_1, J_2, or J_3, perfect squares cannot be completed anymore, and therefore the freedom to fluctuate is restricted. The cMC calculations show that even the smallest non-zero value of J_3 results in a finite critical temperature (however small). On the other hand, for $J_5 > J_4$, no ordering is observed at least up to $J_5/J_4 = 3.5$. The spin structure factors corresponding to the CSL in the tetra-trillium lattice are shown in the left parts of Fig. 4c–e for $T = 0.001J_4$ in cMC.

The analogy between the tetra-trillium and the pyrochlore lattices can be advanced even further. As demonstrated in Fig. 4b, the specific heat per site reaches the value $c_v(T \rightarrow 0) = 0.75$ (without any phase transition) as in the CSL on the pyrochlore lattice, which indicates the absence of quartic modes associated with magnetic order[51]. Furthermore, the specific heat agrees quite well with that of a single tetrahedron, with small deviations occurring at intermediate temperatures $0.1 < T/J4 < 1.0$, implying that the tetra-trillium lattice does not behave simply as a set of decoupled tetrahedra. In the case of the pyrochlore lattice, a U(1) (or Coulomb) CSL is realized, characterized by algebraically decaying correlations and an emergent gauge field that leads to pinch-point singularities in the spin structure factor[3,52]. As shown in Fig. 4, the spin structure factor of the tetra-trillium lattice does not present pinch-point singularities. This absence can be related to the non-bipartite character of the tetra-trillium lattice in terms of tetrahedra. In two dimensions it has been shown that this can lead to a so-called $\mathbb{Z}_2$ CSL, characterized by exponentially decaying correlations down to $T = 0$ and fractionalized magnetic moments[53] (the properties derive actually from the eigenvalues of the adjacency matrix, which are gapped). Exponentially decaying correlations would also explain the negligible finite-size effects in Fig. 4b.

With these arguments, we have established that the classical version of the tetra-trillium model exhibits an extensive ground-state degeneracy and, hence, realizes a CSL. As in models on the pyrochlore lattice, these systems are particularly promising for realizing QSLs when adding quantum fluctuation. This is because quantum effects induce tunneling between the degenerate classical ground states (in our case via the aforementioned 18 spin-flip processes), which may lead to a liquid-like quantum superposition of extensively many classical states. This effect of quantum fluctuations is considerably different from the action of quantum fluctuations on top of a magnetically ordered state, where they merely induce a reduction of the ordered moment. Changing back the classical spins of the tetra-trillium model to $S = 1$ spins (as realized in $K_2Ni_2(SO_4)_3$) is expected to introduce substantial quantum fluctuations, particularly in the present case of isotropic Heisenberg interactions, which are devoid of any easy axis that can facilitate static spins. This fact, together with the observation that the PFFRG spin structure factors for the quantum $S = 1$ case

at $\Lambda = 0.01J_4$ and the cMC results are considerably different (see Fig. 4c–e), evidences that the $S = 1$ tetra-trillium model is no longer a CSL. Nonetheless, quantum fluctuations are unable to select a unique magnetic ground-state out of the degenerate ground-state manifold of the CSL. Hence, the $S = 1$ tetra-trillium model remains magnetically disordered, as indicated by our PFFRG calculations. Taken together, these two observations make a QSL scenario for the $S = 1$ tetra-trillium model plausible. Changing the model parameters of the ideal tetra-trillium system back to the ones realized in $K_2Ni_2(SO_4)_3$ induces weak magnetic order, as seen in experiments and PFFRG. Nevertheless, key features of the spin structure factor of the ideal tetra-trillium system are still seen when simulating the system with the actual material parameters above the ordering transition, as is evident from a comparison between the PFFRG results in Figs. 3 and 4. Therefore, we conclude that the dynamics of $K_2Ni_2(SO_4)_3$ are still substantially governed by the quantum liquidity of the nearby ideal tetra-trillium point.

The evidence of strong dynamics seen in $K_2Ni_2(SO_4)_3$ opens a window of possibilities in search of exotic quantum phases born out of complex 3D lattice geometries beyond the iconic pyrochlore and hyperkagome lattices. Viewing the geometry as a tessellation of tetrahedra on a trillium lattice, we have unveiled a so-far unexplored frustration mechanism at play in the langbeinite family. The excellent agreement between experiment and theory demonstrated for $K_2Ni_2(SO_4)_3$ offers an opportunity to further test the applicability of theoretical concepts to a wider variety of compounds that belong to the langbeinite family. Our theoretical phase diagram identifying an island of liquidity centered around a highly frustrated tetra-trillium lattice provides a valuable guide in search of further promising QSL candidate materials. It is worth mentioning that despite the appearance of magnetic order outside of the identified regime, the ground states remain highly dynamic, thereby allowing for a wide temperature range where emergent phenomena arising out of an interplay between thermal and quantum fluctuations could be explored. An exciting task for future theoretical studies will be to identify possible structures of emergent gauge theories on the tetra-trillium lattice that could underlie the potential QSL behavior. Of particular interest in this context will be how the non-centrosymmetric character of the $P2_13$ (#198) crystallographic space group of $K_2Ni_2(SO_4)_3$ could give rise to a chiral QSL.

Methods
DFT-based energy mapping
We determine the Heisenberg Hamiltonian parameters for the $T = 100$ K structure of $K_2Ni_2(SO_4)_3$ by performing DFT-based energy mapping[54,55] in the same way as was done for the room-temperature structure[22]. We use all electron DFT calculations with the full potential local orbital basis[56] and a generalized gradient approximation (GGA) exchange-correlation functional[57]. We correct for strong electronic correlations on the Ni^{2+} 3d orbitals using a GGA+U functional[58]. We determine the parameters of the Heisenberg Hamiltonian written in the form

$$H = \sum_{i<j} J_{ij} \mathbf{S}_i \cdot \mathbf{S}_j, \qquad (2)$$

where $\mathbf{S}_i$ and $\mathbf{S}_j$ are spin operators and every bond is counted once. We create a $\sqrt{2} \times \sqrt{2} \times 1$ supercell with $P2_1$ space group that allows for eight symmetry-inequivalent spins. This provides 38 distinct energies of different spin configurations and allows us to resolve the eight nearest-neighbor exchange interactions, which we name J_1 to J_8. We choose the relevant value of the interaction U by demanding that the set of interactions match the experimental Curie-Weiss temperature.

Inelastic neutron scattering
Single crystal inelastic neutron scattering data was obtained on the time-of-flight (TOF) instrument LET[59], ISIS (Didcot, UK) using four

different crystals grown from the melt[22]. The crystals, amounting to a total mass of 0.45g, were co-aligned on aluminum posts, to access the (*HHL*) scattering plane. Cadmium shielding was used to reduce the background signal arising from brass and aluminum. The INS measurements were performed at $T = 2$ K, with three different incident energies of $E_i = 2.8$, 5, and 11.7 meV. The (*HHL*) reciprocal space maps were obtained by scanning over an angular range of 140° in 1° steps for 18 h, spending 7.5 min/° for a total of 140 runs. The Horace software was used for visualizing and analyzing the four-dimensional $S(\mathbf{q}, \omega)$ data from the TOF experiment[60]. The single crystal TOF data was symmetrized with respect to symmetry operations in the $P2_13$ space group of $K_2Ni_2(SO_4)_3$[61,62]. In our analysis, we normalized and added together data from different equivalent planes based on the space group symmetries. For the (100) and (110) families of planes we applied 8 symmetry operations to include reflection and inversion symmetries along the two perpendicular axes and about the origin respectively: (x, y, z), (−x, y, z), (x, −y, z), (x, y, −z), (−x, −y, z), (x, −y, −z), (−x, y, -z), (−x, −y, −z). For the (111) family of planes, we applied a 6-fold rotational symmetry.

Classical Monte Carlo

The cMC calculations were carried out using a logarithmic cooling protocol from $T = 2J_4$ down to $T = 0.001J_4$ with 150 temperature steps. Systems of up to $8 \times 12^3 = 13824$ unitary spins are considered. At each temperature, 10^5 cMC steps were performed. Each cMC step consists of N Metropolis trials and N overrelaxation steps intercalated, where N is the number of spins. The acceptance rate of the Metropolis trials is kept at 50% using the adapted Gaussian step[63]. Correlations are calculated over already thermalized states at selected temperatures by doing 4×10^5 cMC steps while measuring correlations once every 100 steps. All results are then averaged over 5 independent runs. The spin structure factors are calculated taking into account the positions of the Ni atoms corresponding to each model, as well as the form factor corresponding to Ni atoms.

Pseudo-fermion functional renormalization group

All results for $S = 1/2$ and $S = 1$ quantum spin models in this paper are obtained by standard PFFRG[32] with the following specifications (general information on the method is provided in Supplementary Note 4). Vertex frequency dependencies are approximated by finite grids with exponentially distributed frequencies. The self-energy is evaluated for 1000 positive frequency arguments. Frequency grids for the two-particle vertex contain 32 positive values for each of the three transfer frequencies. Spin-correlations spanning over distances larger than three lattice constants of the underlying cubic lattice are neglected. After consideration of lattice translation symmetries, this implies the computation of spin-correlations along 1842 lattice vectors, or 622 vectors unrelated by lattice symmetries. For the computation of the phase diagram Fig. 4a, the maximum included correlation vector distance is reduced to two lattice constants, implying 186 vectors unrelated by symmetry. Flow equations are solved by the application of an explicit embedded Runge-Kutta (2, 3) method with adaptive step size[64].

Data availability

Raw data from the neutron scattering experiment was generated at the ISIS, UK, large-scale facility. All the data that support the findings of this study are available in the Zenodo repository (https://doi.org/10.5281/zenodo.12780091).

Code availability

The code for DFT, cMC, and PFFRG calculations of this study is available from the corresponding author upon request.

References

1. Anderson, P. W. Resonating valence bonds: a new kind of insulator? *Mater. Res. Bull.* **8**, 153 (1973).
2. Savary, L. & Balents, L. Quantum spin liquids: a review. *Rep. Prog. Phys.* **80**, 016502 (2016).
3. Henley, C. L. Power-law spin correlations in pyrochlore antiferromagnets. *Phys. Rev. B* **71**, 014424 (2005).
4. Fennell, T. et al. Magnetic Coulomb phase in the spin ice $Ho_2Ti_2O_7$. *Science* **326**, 415 (2009).
5. Benton, O., Jaubert, L. D. C., Yan, H. & Shannon, N. A spin-liquid with pinch-line singularities on the pyrochlore lattice. *Nat. Commun.* **7**, 11572 (2016).
6. Prem, A., Vijay, S., Chou, Y.-Z., Pretko, M. & Nandkishore, R. M. Pinch point singularities of tensor spin liquids. *Phys. Rev. B* **98**, 165140 (2018).
7. Niggemann, N., Iqbal, Y. & Reuther, J. Quantum effects on unconventional pinch point singularities. *Phys. Rev. Lett.* **130**, 196601 (2023).
8. Sachdev, S. Kagomé- and triangular-lattice Heisenberg antiferromagnets: ordering from quantum fluctuations and quantum-disordered ground states with unconfined bosonic spinons. *Phys. Rev. B* **45**, 12377 (1992).
9. Lecheminant, P., Bernu, B., Lhuillier, C., Pierre, L. & Sindzingre, P. Order versus disorder in the quantum Heisenberg antiferromagnet on the kagomé lattice using exact spectra analysis. *Phys. Rev. B* **56**, 2521 (1997).
10. Mila, F. Low-energy sector of the $S = 1/2$ kagome antiferromagnet. *Phys. Rev. Lett.* **81**, 2356 (1998).
11. Kitaev, A. Anyons in an exactly solved model and beyond. *Ann. Phys.* **321**, 2 (2006).
12. Jackeli, G. & Khaliullin, G. Mott insulators in the strong spin-orbit coupling limit: from Heisenberg to a quantum compass and Kitaev models. *Phys. Rev. Lett.* **102**, 017205 (2009).
13. Takagi, H., Takayama, T., Jackeli, G., Khaliullin, G. & Nagler, S. E. Concept and realization of Kitaev quantum spin liquids. *Nat. Rev. Phys.* **1**, 264 (2019).
14. Gingras, M. J. P. & McClarty, P. A. Quantum spin ice: a search for gapless quantum spin liquids in pyrochlore magnets. *Rep. Prog. Phys.* **77**, 056501 (2014).
15. Gao, B. et al. Experimental signatures of a three-dimensional quantum spin liquid in effective spin-1/2 $Ce_2Zr_2O_7$ pyrochlore. *Nat. Phys.* **15**, 1052 (2019).
16. Chern, L. E., Kim, Y. B. & Castelnovo, C. Competing quantum spin liquids, gauge fluctuations, and anisotropic interactions in a breathing pyrochlore lattice. *Phys. Rev. B* **106**, 134402 (2022).
17. Okamoto, Y., Nohara, M., Aruga-Katori, H. & Takagi, H. Spin-liquid state in the $S = 1/2$ hyperkagome antiferromagnet $Na_4Ir_3O_8$. *Phys. Rev. Lett.* **99**, 137207 (2007).
18. Chillal, S. et al. Evidence for a three-dimensional quantum spin liquid in $PbCuTe_2O_6$. *Nat. Commun.* **11**, 2348 (2020).
19. Ghioldi, E. A. et al. Dynamical structure factor of the triangular antiferromagnet: Schwinger boson theory beyond mean field. *Phys. Rev. B* **98**, 184403 (2018).
20. Scheie, A. O. et al. Proximate spin liquid and fractionalization in the triangular antiferromagnet $KYbSe_2$. *Nat. Phys.* **20**, 74 (2024).
21. Scheie, A. O. et al. Nonlinear magnons and exchange Hamiltonians of the delafossite proximate quantum spin liquid candidates $KYbSe_2$ and $NaYbSe_2$. *Phys. Rev. B* **109**, 014425 (2024).
22. Živković, I. et al. Magnetic field induced quantum spin liquid in the two coupled trillium lattices of $K_2Ni_2(SO_4)_3$. *Phys. Rev. Lett.* **127**, 157204 (2021).
23. Yao, W. et al. Continuous spin excitations in the three-dimensional frustrated magnet $K_2Ni_2(SO_4)_3$. *Phys. Rev. Lett.* **131**, 146701 (2023).
24. Boya, K. et al. Signatures of spin-liquid state in a 3D frustrated lattice compound $KSrFe_2(PO_4)_3$ with $S = 5/2$. *APL Mater.* **10**, 101103 (2022).

25. Hopkinson, J. M. & Kee, H.-Y. Geometric frustration inherent to the trillium lattice, a sublattice of the B20 structure. *Phys. Rev. B* **74**, 224441 (2006).
26. Isakov, S. V., Hopkinson, J. M. & Kee, H.-Y. Fate of partial order on trillium and distorted windmill lattices. *Phys. Rev. B* **78**, 014404 (2008).
27. Sibille, R. et al. Coulomb spin liquid in anion-disordered pyrochlore $Tb_2Hf_2O_7$. *Nat. Commun.* **8**, 892 (2017).
28. Hering, M. et al. Phase diagram of a distorted kagome antiferromagnet and application to Y-kapellasite. *npj Comput. Mater.* **8**, 10 (2022).
29. Hagymási, I., Noculak, V. & Reuther, J. Enhanced symmetry-breaking tendencies in the $S = 1$ pyrochlore antiferromagnet. *Phys. Rev. B* **106**, 235137 (2022).
30. Noculak, V. et al. Classical and quantum phases of the pyrochlore $S = \frac{1}{2}$ magnet with Heisenberg and Dzyaloshinskii-Moriya interactions. *Phys. Rev. B* **107**, 214414 (2023).
31. Kiese, D. et al. Pinch-points to half-moons and up in the stars: the kagome skymap. *Phys. Rev. Res.* **5**, L012025 (2023).
32. Müller, T. et al. Pseudo-fermion functional renormalization group for spin models. *Rep. Prog. Phys.* **87**, 036501 (2024).
33. Iqbal, Y., Thomale, R., Parisen Toldin, F., Rachel, S. & Reuther, J. Functional renormalization group for three-dimensional quantum magnetism. *Phys. Rev. B* **94**, 140408 (2016).
34. Kulagin, S. A., Prokof'ev, N., Starykh, O. A., Svistunov, B. & Varney, C. N. Bold diagrammatic Monte Carlo method applied to fermionized frustrated spins. *Phys. Rev. Lett.* **110**, 070601 (2013).
35. Huang, Y., Chen, K., Deng, Y., Prokof'ev, N. & Svistunov, B. Spin-ice state of the quantum Heisenberg antiferromagnet on the pyrochlore lattice. *Phys. Rev. Lett.* **116**, 177203 (2016).
36. Wang, T., Cai, X., Chen, K., Prokof'ev, N. V. & Svistunov, B. V. Quantum-to-classical correspondence in two-dimensional Heisenberg models. *Phys. Rev. B* **101**, 035132 (2020).
37. Schneider, B. and Sbierski, B. Taming spin susceptibilities in frustrated quantum magnets: mean-field form and approximate nature of the quantum-to-classical correspondence. https://arxiv.org/abs/2407.09401 (2024).
38. Trumper, A. E., Manuel, L. O., Gazza, C. J. & Ceccatto, H. A. Schwinger-Boson approach to quantum spin systems: Gaussian fluctuations in the "natural" gauge. *Phys. Rev. Lett.* **78**, 2216 (1997).
39. Jiang, H.-C., Yao, H. & Balents, L. Spin liquid ground state of the spin-$\frac{1}{2}$ square J_1-J_2 Heisenberg model. *Phys. Rev. B* **86**, 024424 (2012).
40. Hu, W.-J., Becca, F., Parola, A. & Sorella, S. Direct evidence for a gapless Z_2 spin liquid by frustrating Néel antiferromagnetism. *Phys. Rev. B* **88**, 060402 (2013).
41. Wang, L. & Sandvik, A. W. Critical level crossings and gapless spin liquid in the square-lattice spin-1/2 J_1 – J_2 Heisenberg antiferromagnet. *Phys. Rev. Lett.* **121**, 107202 (2018).
42. Nomura, Y. & Imada, M. Dirac-type nodal spin liquid revealed by refined quantum many-body solver using neural-network wave function, correlation ratio, and level spectroscopy. *Phys. Rev. X* **11**, 031034 (2021).
43. Liu, W.-Y. et al. Gapless quantum spin liquid and global phase diagram of the spin-1/2 J_1-J_2 square antiferromagnetic Heisenberg model. *Sci. Bull.* **67**, 1034 (2022).
44. Hu, W.-J., Gong, S.-S., Zhu, W. & Sheng, D. N. Competing spin-liquid states in the spin-$\frac{1}{2}$ Heisenberg model on the triangular lattice. *Phys. Rev. B* **92**, 140403 (2015).
45. Zhu, Z. & White, S. R. Spin liquid phase of the $S = \frac{1}{2}$ J_1 – J_2 Heisenberg model on the triangular lattice. *Phys. Rev. B* **92**, 041105 (2015).
46. Saadatmand, S. N. & McCulloch, I. P. Symmetry fractionalization in the topological phase of the spin-$\frac{1}{2}$ J_1 – J_2 triangular Heisenberg model. *Phys. Rev. B* **94**, 121111 (2016).
47. Iqbal, Y., Hu, W.-J., Thomale, R., Poilblanc, D. & Becca, F. Spin liquid nature in the Heisenberg J_1 – J_2 triangular antiferromagnet. *Phys. Rev. B* **93**, 144411 (2016).
48. Oitmaa, J. Magnetic phases in the J_1 – J_2 Heisenberg antiferromagnet on the triangular lattice. *Phys. Rev. B* **101**, 214422 (2020).
49. Gonzalez, M. G., Ghioldi, E. A., Gazza, C. J., Manuel, L. O. & Trumper, A. E. Interplay between spatial anisotropy and next-nearest-neighbor exchange interactions in the triangular Heisenberg model. *Phys. Rev. B* **102**, 224410 (2020).
50. Qian, X. & Qin, M. Absence of spin liquid phase in the J_1 – J_2 Heisenberg model on the square lattice. *Phys. Rev. B* **109**, L161103 (2024).
51. Moessner, R. & Chalker, J. T. Properties of a classical spin liquid: the Heisenberg pyrochlore antiferromagnet. *Phys. Rev. Lett.* **80**, 2929 (1998).
52. Isakov, S. V., Gregor, K., Moessner, R. & Sondhi, S. L. Dipolar spin correlations in classical pyrochlore magnets. *Phys. Rev. Lett.* **93**, 167204 (2004).
53. Rehn, J., Sen, A. & Moessner, R. Fractionalized $\mathbb{Z}_2$ classical Heisenberg spin liquids. *Phys. Rev. Lett.* **118**, 047201 (2017).
54. Iqbal, Y. et al. Signatures of a gearwheel quantum spin liquid in a spin-$\frac{1}{2}$ pyrochlore molybdate Heisenberg antiferromagnet. *Phys. Rev. Mater.* **1**, 071201(R) (2017).
55. Fujihala, M. et al. Birchite $Cd_2Cu_2(PO_4)_2SO_4 \cdot 5H_2O$ as a model antiferromagnetic spin-1/2 Heisenberg J_1-J_2 chain. *Phys. Rev. Mater.* **6**, 114408 (2022).
56. Koepernik, K. & Eschrig, H. Full-potential nonorthogonal local-orbital minimum-basis band-structure scheme. *Phys. Rev. B* **59**, 1743 (1999).
57. Perdew, J. P., Burke, K. & Ernzerhof, M. Generalized gradient approximation made simple. *Phys. Rev. Lett.* **77**, 3865 (1996).
58. Liechtenstein, A. I., Anisimov, V. I. & Zaanen, J. Density-functional theory and strong interactions: orbital ordering in Mott-Hubbard insulators. *Phys. Rev. B* **52**, R5467 (1995).
59. Bewley, R., Taylor, J. & Bennington, S. LET, a cold neutron multi-disk chopper spectrometer at ISIS. *Nucl. Instrum. Methods Phys. Res. Sect. A* **637**, 128 (2011).
60. Ewings, R. et al. Horace: software for the analysis of data from single crystal spectroscopy experiments at time-of-flight neutron instruments. *Nucl. Instrum. Methods Phys. Res. Sect. A* **834**, 132 (2016).
61. $K_2Ni_2(SO_4)_3$ ($K_2Ni_2[SO_4]_3$) crystal structure: datasheet from "PAULING FILE Multinaries Edition – 2022" (2023).
62. Hikita, T., Sekiguchi, H. & Ikeda, T. Phase transitions in new langbeinite-type crystals. *J. Phys. Soc. Jpn.* **43**, 1327 (1977).
63. Alzate-Cardona, J. D., Sabogal-Suárez, D., Evans, R. F. L. & Restrepo-Parra, E. Optimal phase space sampling for Monte Carlo simulations of Heisenberg spin systems. *J. Phys. Condens. Matter* **31**, 095802 (2019).
64. Galassi, M. et al. GNU Scientific Library reference manual (3rd Ed.) (Network Theory Ltd., 2009).

Author contributions

Single crystals were grown by A.M. Inelastic neutron scattering data were measured and analyzed by A.S., V.F., J.-R.S., R.B., H.M.R., and I.Ž. Classical Monte Carlo calculations were carried out by M.G.G. and J.R. Pseudo-fermion functional renormalization-group calculations were carried out by V.N. and J.R. Energy mappings based on DFT were carried out by H.O.J. Analytical calculations on the tetra-trillium lattice were carried out by M.G.G., V.N., J.R., and Y.I. The manuscript was written by M.G.G. and I.Ž. with contributions from all co-authors.

Competing interests

The authors declare no competing interests.

Additional information

Supplementary information The online version contains supplementary material available at https://doi.org/10.1038/s41467-024-51362-1.